

Competition between capillarity, layering and biaxiality in a confined liquid crystal

S. Varga^{1a}, Y. Martínez-Ratón², and E. Velasco³

¹ Departamento de Física Teórica de la Materia Condensada, Universidad Autónoma de Madrid, E-28049 Madrid, Spain

² Grupo Interdisciplinar de Sistemas Complejos (GISC), Departamento de Matemáticas, Escuela Politécnica Superior, Universidad Carlos III de Madrid, Avenida de la Universidad 30, E-28911, Leganés, Madrid, Spain

³ Departamento de Física Teórica de la Materia Condensada and Instituto de Ciencia de Materiales Nicolás Cabrera, Universidad Autónoma de Madrid, E-28049 Madrid, Spain

Abstract. The effect of confinement on the phase behaviour and structure of fluids made of biaxial hard particles (cuboids) is examined theoretically by means of Onsager second-order virial theory in the limit where the long particle axes are frozen in a mutually parallel configuration. Confinement is induced by two parallel planar hard walls (slit-pore geometry), with particle long axes perpendicular to the walls (perfect homeotropic anchoring). In bulk, a continuous nematic-to-smectic transition takes place, while shape anisotropy in the (rectangular) particle cross section induces biaxial ordering. As a consequence, four bulk phases, uniaxial and biaxial nematic and smectic phases, can be stabilised as the cross-sectional aspect ratio is varied. On confining the fluid, the nematic-to-smectic transition is suppressed, and either uniaxial or biaxial phases, separated by a continuous transition, can be present. Smectic ordering develops continuously from the walls for increasing particle concentration (in agreement with the suppression of nematic-smectic second order transition at confinement), but first-order layering transitions, involving structures with n and $n+1$ layers, arise in the confined fluid at high concentration. Competition between layering and uniaxial-biaxial ordering leads to three different types of layering transitions, at which the two coexisting structures can be both uniaxial, one uniaxial and another biaxial, or both biaxial. Also, the interplay between molecular biaxiality and wall interactions is very subtle: while the hard wall disfavours the formation of the biaxial phase, biaxiality is against the layering transitions, as we have shown by comparing the confined phase behaviour of cylinders and cuboids. The predictive power of Onsager theory is checked and confirmed by performing some calculations based on fundamental-measure theory.

PACS. XX.XX.XX No PACS code given

1 Introduction

The behaviour of confined nematics is a problem of great fundamental and practical interest. Nematic materials exhibit strong responses to even subtle external or surface fields, which are used in various technological applications. In general, confinement into a narrow planar slit pore induces competing capillary and layering transitions at low temperature or high concentration. Recent theoretical works have shown that these phenomena lead to complex phase behaviour in confined lamellar or smectic phases in three [1,2,3] and two [4] dimensions. Classical techniques [5,6,7] and novel atomic-force microscopy have been used to study capillary nematization [8,9] and the pre-smectic regime [10], but the strong smecticization regime, where layering and commensuration effects are crucial, is yet to be experimentally studied.

Another fascinating topic in the field of liquid crystals is the search for biaxial nematic phases [11] (for a recent review, see Berardi et al. [12]). The recent discovery of biaxial nematics in bent-core molecules [13,14] has renewed the interest in biaxiality and in the question of what the minimum molecular interaction requirements are for bulk biaxial nematic stability. Several factors, such as hydrogen bonding, influence the stability of the biaxial ordering [15]. The onset of biaxiality and the development of long-range bulk biaxial order may also be greatly affected by the presence of a surface, a situation where nontrivial coupling between biaxiality and surface interactions may occur. Surfaces may induce biaxial phases in one-component fluids [16,17,18] and in mixtures [19]. In addition, confinement may induce smectic-like stratification of the fluid, which may be coupled to biaxial ordering. Therefore, the interplay between biaxiality and the capillary nematic-smectic transition, and/or layering transitions deep in the smectic regime, is expected to yield interesting physics, and is the topic of the present paper.

^a Permanent address: Institute of Physics, University of Pannonia, P.O. Box 158, Veszprém H-8201, Hungary.

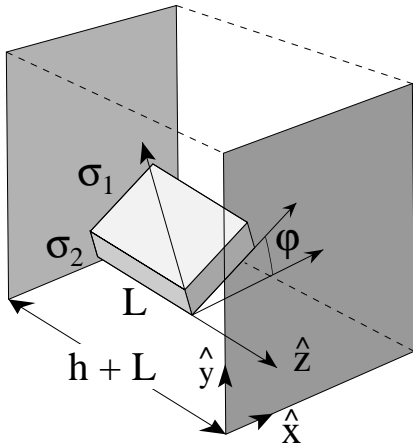


Fig. 1. Schematic of particle shape and lengths, and geometry used in the confined fluid.

Many studies have been devoted to investigate how the bulk phenomenology of liquid crystals is affected by strong confinement and surface interactions [20, 21, 22], which may promote or discourage layering and biaxiality inside the pore. Up to now microscopic models have been scarcely used to address this issue. Elastic theory has been employed to discuss the anchoring energy in a biaxial nematic phase (see e.g. [23]). The phenomenological Landau-de Gennes theory has been extensively used to study uniaxial and biaxial nematics in films under various conditions [24, 25, 26, 27, 28, 29, 30, 31, 32, 33, 34, 35, 36], and also specifically in connection with the biaxial transition taking place in a thin nematic layer subject to antagonistic easy axes in the two surfaces [37, 38, 39, 40] (the so-called hybrid cell). Experimental verification of this phenomenon now exists [41]. The presmectic film [42] and fully developed confined smectics [43] were also considered. Models dealing only with attractive particle interactions (of the Maier-Saupe type) have also been used for confined nematic liquid crystals [44, 45, 46, 47]. Theories on lattice models [21, 48, 49] and computer simulations on lattice [50, 51, 52, 53] and continuous [54, 55, 56, 57, 58, 59, 60, 61] models are also abundant. In all these studies the issue of biaxiality is implicitly or explicitly considered.

Density-functional theory (DFT) allows us to study the properties of inhomogeneous fluids from molecular interactions. DFT has been used to study confined nematics from a more microscopic perspective [62, 63, 64, 65, 66, 67]. A number of studies based on DFT have focused on confined nematic phases between symmetric [68, 69, 70, 64] and asymmetric [61] substrates, and also confined smectic phases [3, 71] have been studied. All of these DFT studies considered only uniaxial, but not biaxial, particles. Since DFT gives a direct link between particle shape and phase biaxiality, it is a very powerful technique to investigate confined biaxial nematics and will be the tool used in the present work.

All mesogenic molecules are biaxial to some extent. Therefore, microscopic studies of idealised biaxial particle models in strong confinement and subject to particular

surface interactions seem pertinent. Following Vanakaras et al. [72], we have recently investigated the bulk phase behaviour of a simplified athermal model for biaxial particle, consisting of hard cuboids of lengths $\sigma_2 < \sigma_1 < L$, with frozen orientation in the long molecular axes (z axis, see Fig. 1). We used a sophisticated free-energy density functional based on the fundamental-measure concepts [73]. The shape of these particles effectively describes bent-core molecules, with the angle of aperture being related to the cross-sectional aspect ratio $\kappa = \sigma_1/\sigma_2 > 1$ of the cuboids. In this model, there is always a primary nematic director \hat{z} , parallel to the particle long axes; but a second director may arise in the xy plane, associated with a nonuniform distribution in the azimuthal angle φ . In this case a biaxial phase appears. In line with the findings of Vanakaras et al. [72], based on Onsager theory, we found, in both the nematic and smectic regions of phase stability, uniaxial and biaxial phases, with a complex bulk phase diagram exhibiting continuous transition curves meeting at a four-phase point.

Here we use the same Onsager theory as in Ref. [72], since it is much simpler than our previous theory [73], but predicts essentially the same qualitative behaviour. The bulk phase diagram in the plane chemical potential μ (or scaled particle concentration c_0) versus aspect ratio of the particle cross section κ , is shown in Fig. 2 (see later for a more comprehensive discussion). The four bulk phases identified are: uniaxial nematic (N), biaxial nematic (N_B), uniaxial smectic (S), and biaxial smectic (S_B). Depending on the value of κ , biaxiality may arise in the nematic phase (for large aspect ratios) directly from the uniaxial nematic, or require as a prerequisite the formation of smectic layers, giving rise to a biaxial smectic.

In this work hard walls will be used to confine the fluid, promoting perfect homeotropic anchoring (long particle axes perpendicular to the walls, Fig. 1). The walls do not couple to the azimuthal angle φ , so that the second director, whenever there is one, can be taken to be aligned in a fixed direction, say the \hat{x} axis (i.e. both walls have identical easy axes; the case with different easy axes will be the subject of a future publication). As will be seen later, a hard wall turns out to have a disordering effect with respect to biaxiality. As a consequence, biaxial phases grow in the central region of the slab, not near the surfaces, and occur at higher pressure/chemical potential than in bulk. However, as common in adsorption problems involving hard interactions, the opposite effect occurs for the smectic order parameter, which is reinforced near the walls, so that strong layering may occur below bulk saturation. Layering transitions, associated with commensuration effects between pore width and smectic period, are disfavoured by biaxiality. The capillary biaxiality transition interacts with the layering transitions in interesting ways, giving rise to three types of layering transitions, involving two biaxial, one uniaxial and another biaxial, or both uniaxial, coexisting structures, differing by a single layer. Even though the biaxial bulk transition survives to confinement, the continuous bulk nematic-smectic transition is suppressed under confinement, so that the con-

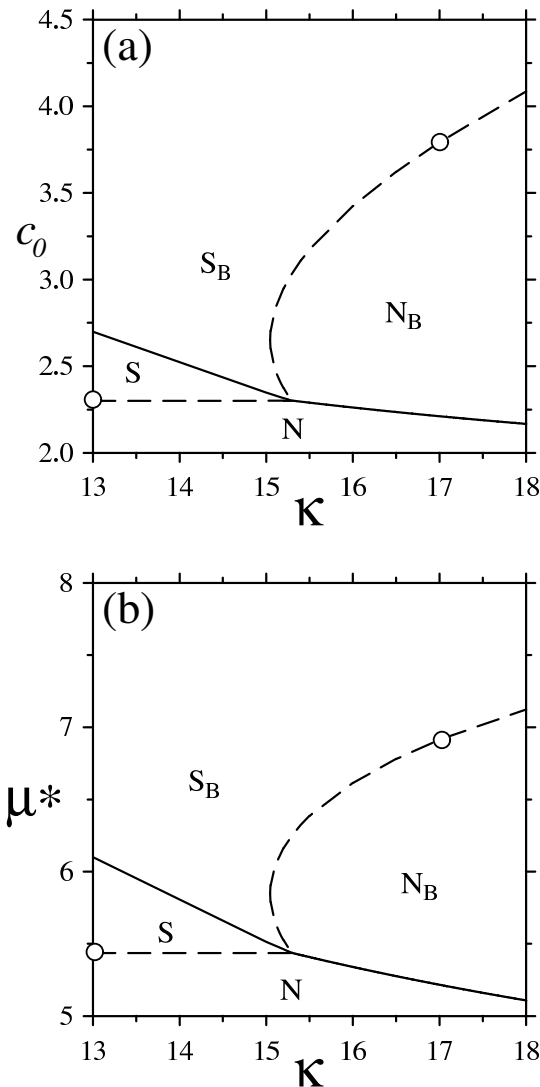


Fig. 2. Bulk phase diagram of hard cuboids as obtained from Onsager theory. (a) Density c_0 (scaled with second virial coefficient B_2) vs. cross-sectional aspect ratio κ , and (b) reduced chemical potential μ^* vs. κ . Curves show the boundary between the different phases. Dashed curves indicate transitions that disappear on confinement. All phase transitions are continuous. Labels indicate stable phases. The corresponding bulk N-S transitions of the two confined fluids studied are indicated by circles.

confined nematic smoothly transforms into a confined smectic phase; here confined smectic phases are identified by their propensity to undergo layering transitions at high values of chemical potential. Each of these (infinitely large in number) first-order layering transitions disappears at a critical point.

Two different scenarios, corresponding to two different choices for aspect ratio, will be presented: $\kappa = 13$ and $\kappa = 17$. To explain these two choices, we again use Fig. 2 which represents the bulk phase diagram in the reduced chemical potential $\mu^* = \beta\mu$, or scaled particle concentration c_0 , versus aspect ratio κ plane. All bulk phase

transitions are continuous and meet at a four-phase point. The derivatives of the transition densities with respect to the aspect ratio at different sides of the four-phase point are different for the four transition lines. The continuous nematic-to-smectic transitions, N-S and N_B-S_B, are suppressed under confinement (this is indicated by dashed curves). The uniaxial (U)-to-biaxial (B) phase transition (which, depending on the value of κ , is associated with either the N-N_B or S-S_B bulk transitions) survives (this is indicated by the continuous curves), and becomes a wavy line as the wall separation h (see Fig. 1) is varied; its average location is shifted to higher values of μ due to the disordering effect of the walls. However, even though the bulk nematic-to-smectic bulk transition disappears on confinement, it governs the behaviour of the layering critical points, since the latter tend to the bulk nematic-to-smectic chemical potential as the slit-pore is made wider. In one case considered ($\kappa = 13$), the relevant bulk transition is N-S, while in the other ($\kappa = 17$) layering transitions are governed by the N_B-S_B bulk transition (open circles in Fig. 2). In addition, when the U-B transition is above the bulk N-S transition ($\kappa < 15.304$), layering transitions intersect with the U-B transition curve, whereas in the opposite case the two transitions are independent.

The outline of the paper is as follows. In Section 2 the model system and the theory are presented. The phase diagrams of bulk and confined systems and the equilibrium density and order parameter profiles are shown and discussed in Section 3. In Section 4 we make some concluding remarks. Finally, we present a bifurcation analysis for the N-S, N-N_B and U-B phase transitions in the Appendix, and an explanation for the emergence of biaxial ordering near the S-S_B transition.

2 Theory

We study the effect of confinement on the phase behaviour of a fluid of biaxial hard particles. The appropriate thermodynamic free energy for confined fluids in DFT is the grand-canonical free-energy functional per unit area $\Omega[\rho]/A$, which in our case is given by

$$\frac{\Omega[\rho]}{A} = \frac{F[\rho]}{A} - \int dz \int d\varphi \rho(z, \varphi) [\mu - V_{\text{ext}}(z, \varphi)], \quad (1)$$

where $\rho(z, \varphi)$ is the position- and orientation- dependent local number density, and $V_{\text{ext}}(z, \varphi)$ is the external potential. In Eqn. (1) the Helmholtz free-energy functional is the sum of ideal and excess contributions, $F[\rho] = F_{\text{id}}[\rho] + F_{\text{ex}}[\rho]$, and can be written as

$$\begin{aligned} \frac{\beta F_{\text{id}}[\rho]}{A} &= \int dz \int d\varphi \rho(z, \varphi) [\log(\rho(z, \varphi) A^3) - 1], \\ \frac{\beta F_{\text{ex}}[\rho]}{A} &= -\frac{1}{2} \int dz_1 \int d\varphi_1 \int dz_2 \int d\varphi_2 \rho(z_1, \varphi_1) \\ &\quad \times \rho(z_2, \varphi_2) \tilde{f}(z_{12}, \varphi_{12}), \end{aligned} \quad (2)$$

where Λ is the thermal wavelength and $\tilde{f}(z_{12}, \varphi_{12})$ is the integrated Mayer function over the $x-y$ plane, with $z_{12} = z_1 - z_2$ and $\varphi_{12} = \varphi_1 - \varphi_2$. We set $\Lambda = 1$ since this does not affect the fluid phase behaviour. Note that, while the ideal contribution is exact, the excess part is approximated at the level of second-order virial theory. Particles are confined between two parallel hard walls, the effect of which is modelled by an external potential,

$$\beta V_{\text{ext}}(z, \varphi) = \begin{cases} \infty, & z < 0, \\ 0, & 0 \leq z \leq h, \\ \infty, & z > h, \end{cases} \quad (3)$$

where $h + L$ is the distance between the walls, and the normal to the wall is along the z direction. This wall-particle interaction confines the centre of mass of the particles to stay in the finite interval $0 \leq z \leq h$. Since the cross section of the cuboid is a rectangle, it is sufficient to consider the interval $0 \leq \varphi \leq \pi$. Due to the exclusion interaction between the wall and the particles, we have $\rho(z, \varphi) = 0$ for $z < 0$ and $z > h$. The use of frozen orientations for the long particle axes substantially simplifies the calculations. This approximation may be valid in a very dense mesogenic system with perfect homeotropic anchoring (homeotropic anchoring could be achieved by means of very strong external electric/magnetic fields or by special surface treatments leading to specific wall-particle interactions). After all these assumptions, the grand canonical free energy functional per unit volume can be simplified to give

$$\frac{\Omega[\rho]}{V} = \frac{F[\rho]}{V} - \frac{\mu}{h} \int_0^h dz \rho(z), \quad (4)$$

where

$$\rho(z) = \int_0^\pi d\varphi \rho(z, \varphi). \quad (5)$$

The ideal and excess free-energy contributions become

$$\begin{aligned} \frac{\beta F_{\text{id}}[\rho]}{V} &= \frac{1}{h} \int_0^h dz \int_0^\pi d\varphi \rho(z, \varphi) \{ \log [\rho(z, \varphi)] - 1 \}, \\ \frac{\beta F_{\text{exc}}[\rho]}{V} &= \frac{1}{2h} \int_0^h dz_1 \int_0^\pi d\varphi_1 \rho(z_1, \varphi_1) \int_{z_1-a(z_1)}^{z_1+b(z_1)} dz_2 \\ &\quad \times \int_0^\pi d\varphi_2 \rho(z_2, \varphi_2) A_{\text{ex}}(z_{12}, \varphi_{12}), \end{aligned} \quad (6)$$

where the functions $a(z)$ and $b(z)$ are defined by

$$a(z) = \begin{cases} z, & 0 \leq z \leq L, \\ L, & z > L, \end{cases} \quad (7)$$

$$b(z) = \begin{cases} L, & z \leq h - L, \\ h - z, & h - L < z \leq h. \end{cases} \quad (8)$$

$A_{\text{ex}}(z, \varphi)$ is the excluded area between the cross sections of two particles. Functional minimization of Eqn. (4) with respect to the local density at fixed chemical potential provides the equilibrium density profile of the fluid. The resulting integral equation for $\rho(z, \varphi)$ is

$$\begin{aligned} \rho(z_1, \varphi_1) &= e^{\beta\mu - \int_{z_1-a(z_1)}^{z_1+b(z_1)} dz_2 \int_0^\pi d\varphi_2 \rho(z_2, \varphi_2) A_{\text{ex}}(z_{12}, \varphi_{12})} \\ &= e^{\beta\mu - \int_{z_1-a(z_1)}^{z_1+b(z_1)} dz_2 \int_0^\pi d\varphi_2 \rho(z_2, \varphi_2) A_{\text{ex}}(z_{12}, \varphi_{12})} \end{aligned} \quad (9)$$

The inputs to the above equation are the chemical potential μ and the wall separation h . The excluded area between two cuboids is given by

$$\begin{aligned} A_{\text{ex}}(z, \varphi) &= [2\sigma_1\sigma_2(1 + |\cos \varphi|) + (\sigma_1^2 + \sigma_2^2)|\sin \varphi|] \\ &\quad \times \Theta(L - |z|). \end{aligned} \quad (10)$$

We have solved Eqn. (9) using two methods. One is the standard iterative procedure, which was applied in the case of wide pores. The other is the Fourier expansion method, used for narrow pores. The choice of method was dictated by the need to optimise computation time, but both give numerically identical results in a wide range of pore sizes.

The properties of the bulk smectic fluid can also be calculated by solving Eqn. (9) at fixed chemical potential and fixed value of h [in the case of the nematic, we simply evaluate (4)-(8) for $\rho(z, \varphi) = \rho_0 = N/V$, the mean density]. For the bulk phases, the $a(z)$ and $b(z)$ functions have to be defined as $a(z) = b(z) = L$, and periodic boundary conditions are applied for $\rho(z, \varphi)$ along the z direction in the case of the smectic phase. The value of h that minimizes the grand potential is identified with the smectic period d , while the corresponding density distribution is the equilibrium density distribution of the smectic phase. In the following, the particle length (long axis) L is used as unit length, so that the scaled pore width and the z coordinate are $h^* = h/L$ and $z^* = z/L$, respectively. In the case of density, a more convenient unit of volume is the second virial coefficient of the particles in the uniaxial nematic phase, which is given by $B_2 = LA_{\text{ex}}^{(0)}$, where $A_{\text{ex}}^{(0)} = \pi^{-1} \int_0^\pi d\varphi A_{\text{ex}}(0, \varphi)$. The scaled bulk density will be $c_0 = \rho_0 B_2$. With this choice the bulk uniaxial nematic-smectic transition density is independent of the geometry and shape anisotropy of the cross section (see A.1).

Eqn. (9) furnishes the density profile at given chemical potential for a particular value of transverse aspect ratio. This density profile can be either uniaxial or biaxial, both in bulk and in the confined cases. It may also happen that more than one solution exists for a given input. Therefore an analysis of the grand potential is necessary to find the stable phase and possible phase transitions. In the next section we present the bulk and confined phase diagrams, as well as density profiles, as obtained from the method explained above.

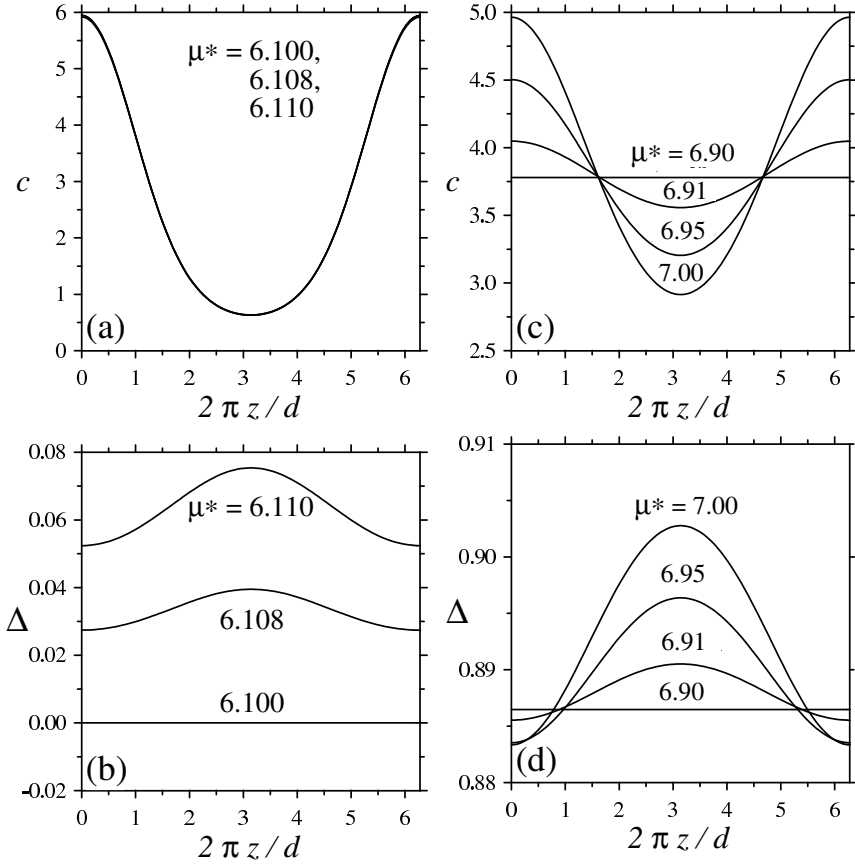


Fig. 3. Density profile and biaxial order parameter in the vicinity of the S-S_B transition ((a) and (b)), and N_B-S_B transition ((c) and (d)) for hard cuboids. The aspect ratio of the particle cross section is $\kappa = 13$ in (a) and (b), and $\kappa = 17$ in (c) and (d). The values of the corresponding chemical potentials are shown in the figures.

3 Results and discussion

3.1 Bulk behaviour

The bulk phase diagram of the parallel hard-cuboid fluid has already been determined by both Onsager theory [72] and Fundamental-Measure theory (FMT) [73]. The main focus of those studies was to determine the effect of the cross-sectional aspect ratio on the stability of biaxial ordering against uniaxial ordering. It was found that macroscopic biaxial ordering can be enhanced with increasing aspect ratio κ . The theories agree qualitatively, in that both predict continuous uniaxial nematic-uniaxial smectic (N-S), uniaxial smectic-biaxial smectic (S-S_B), uniaxial nematic-biaxial nematic (N-N_B), and biaxial nematic-biaxial smectic (N_B-S_B) phase transitions, all meeting at a four-phase point located at (κ_4, μ_4) . However, the transition lines and the location of the four-phase point, and therefore the onset of N_B stability, are different in the two theories; for example, Onsager theory predicts $\kappa_4 = 15.304$, while $\kappa_4 = 18.101$ with FMT. Nevertheless, it is quite surprising that a second-order virial theory such as Onsager's works quite well, even in the highly ordered smectic phase. Later in this section we show that Onsager

and FMT theories also produce very similar density profiles in the confined system.

As a first step, we recalculated the bulk phase diagram, which is a useful reference to discuss the properties of the confined fluid and its connection to bulk behaviour. Starting from a high value of μ , and performing minimisations for decreasing values, the nematic-smectic phase boundary for a given aspect ratio κ can be obtained when the equilibrium density distribution becomes independent of z . In addition, we performed N-S and N-N_B bifurcation analyses (see A.1 and A.2 for details), the results of which agree perfectly well with those from the minimisations. Using c_0 as scaled density, the value of density at the boundary, c_0^{NS} , is independent of both aspect ratio and even shape of the particle cross section. The resulting equation for the N-S transition density is

$$c_0^{\text{NS}} = -[2j_0(x^*)]^{-1}, \quad (11)$$

where $\pi < x^* < 3\pi/2$ is the solution of the trascendental equation $\tan x = x$. The phase diagram is depicted in Fig. 2. In the calculations that follow, we have chosen two significantly different model systems: $\kappa = 13$ and 17. As can be seen from the figure, these two systems have different phase sequences with increasing chemical potential (density): N \rightarrow S \rightarrow S_B for $\kappa = 13$, and N \rightarrow N_B \rightarrow S_B for the more

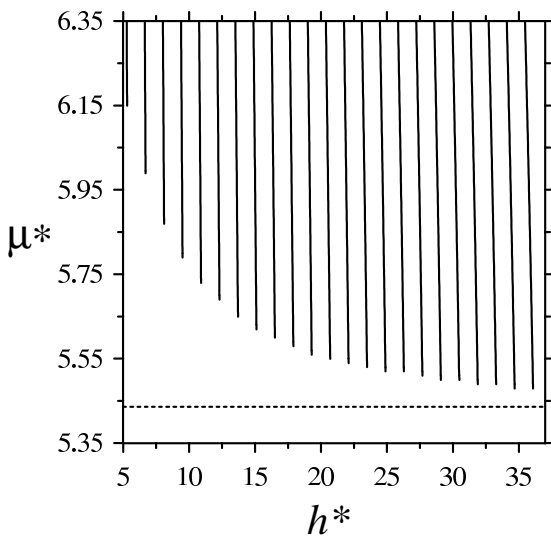


Fig. 4. Phase diagram of confined hard cylinders. Phase boundaries of the layering transitions in the chemical potential μ vs. pore width h plane. The dashed line corresponds to the chemical potential of the bulk N-S transition. The layering transition in the widest pore examined takes place between the structures with 26 and 27 layers.

anisotropic system ($\kappa = 17$). In Fig. 3 the local scaled density $c(z)$ and biaxial order parameter $\Delta(z)$, defined as

$$c(z) = \frac{B_2}{\pi} \int_0^\pi d\varphi \rho(z, \varphi),$$

$$\Delta(z) = \frac{1}{\rho(z)} \int_0^\pi d\varphi \cos 2\varphi \rho(z, \varphi), \quad (12)$$

are plotted as a function of z along one smectic period. The evolution of these quantities with μ is quite interesting. For example, the system with $\kappa = 13$ undergoes a S-S_B transition at $\mu^* = 6.1$, but the density profile hardly changes with increasing μ , while biaxial order develops quickly. A remarkable behaviour of the biaxial ordering is that it peaks in the middle of the interstitial region, which means that particles are more ordered between neighboring layers than inside the layers. A detailed explanation for this behaviour, which was already noticed in our previous FMT study [73], is provided in Sec. A.4. Regarding the N_B-S_B transition of the $\kappa = 17$ system [Figs. 3(c) and (d)], it takes place at $\mu^* = 6.9$, with $c_0 = 3.78$ and a biaxial order parameter $\Delta_0 = 0.886$. Both the density and the biaxial profiles change substantially on the smectic side. As in the previous case, the density and biaxial profiles are out-of-phase and, interestingly, the in-layer biaxial order decreases slightly with increasing chemical potential. This is evidently due to the more efficient packing in the smectic phase.

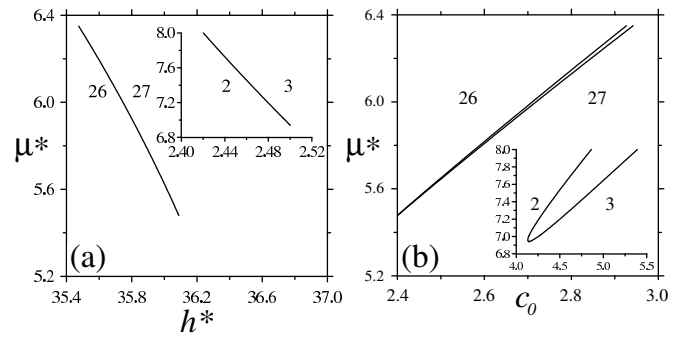


Fig. 5. Phase diagram of confined hard cylinders. (a) μ^* - h^* phase diagram in the region of the 26-27 layering transition. Inset shows the 2-3 layering transition. (b) Reduced chemical potential μ^* vs. coexistence mean densities c_0 for the 26-27 layering transition. Inset shows the 2-3 layering transition.

3.2 Behaviour under confinement

3.2.1 Hard cylinders

We start by discussing a simpler fluid, that of parallel hard cylinders. This fluid only undergoes a single transition in bulk, the N-S transition, and does not exhibit any biaxial phase (the solid phase is not considered in the present study). Due to suppression of long-range smectic fluctuations, the N-S transition vanishes in the confined case. However first-order layering transitions do take place. At a layering transition, two smectic-like structures, having n and $n+1$ layers, coexist at the same pore width, which can accommodate slightly compressed or swollen structures. The phase diagram is shown in Fig. 4 in the μ - h plane for a wide range of pore widths. Since more and more layers can accommodate into the slit pore with increasing pore width, the number of layering transition is infinite in the limit $h \rightarrow \infty$. We can see that the layering transition curves are almost straight and vertical in the μ - h plane. However, the slope decreases slightly with pore width. The distance between two consecutive transition curves is about $1.35L$ (with L the length of the cylinders), and all curves terminate in lower critical points. The dependence of the location of these critical points on h shows that the layering transitions can be stabilized with increasing pore width. In addition, values of the critical chemical potentials (or densities) converge to the bulk N-S value μ_{NS} with increasing pore width. The shape of the layering transition curves is highlighted in Fig. 5(a) by showing two extreme cases: the regions around the 2-3 and 26-27 layering transitions. The transition curves are very steep, but they are convex in very narrow pores and concave in wide pores. The dependence of the coexisting average densities with μ is shown in Fig. 5(b), where c_0 is defined as $c_0 = h^{-1} \int_0^h dz c(z)$. It is clear that the density gap between coexisting layered structures shrinks with increasing pore width. This is due to the fact that the contribution from wall-particle interactions decreases relative to that from particle-particle interactions, i.e. the

wall has less effect on the structure in the middle of the pore.

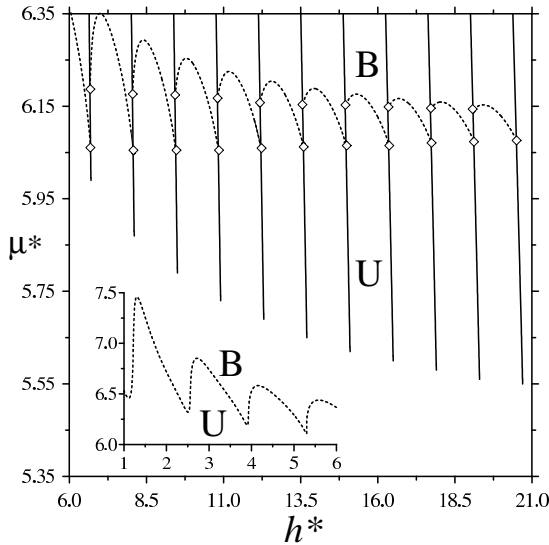


Fig. 6. Phase diagram of confined hard cuboids in the μ^* - h^* plane. Layering transitions are indicated by continuous curves, while the uniaxial-biaxial phase is indicated by a dashed curve. Inset shows the uniaxial-biaxial phase transition for narrow pores. U and B denote uniaxial and biaxial phases, respectively. Diamonds indicate the intersection between the uniaxial-biaxial and layering transitions. The value of the cross-sectional aspect ratio is $\kappa = 13$.

3.2.2 Hard cuboids

In the case of confined hard cuboids again there is no N-S transition. However, by contrast with the previous case, there is a uniaxial-to-biaxial (U-B) phase transition. Therefore only one type of (continuous) ordering transition can take place. The phase diagram of confined cuboids is shown in Fig. 6. While the layering transition curves are obtained by searching for two solutions of the Euler-Lagrange equation, Eqn. (9), with equal grand potentials, the U-B phase boundary was obtained from the numerical solution of the set of bifurcation equations derived in A.3 [see Eqns. (20), (22) and (23)]. The U-B transition line $\mu_{UB}(h)$ is an oscillatory function of pore width that asymptotically tends to the bulk S-SB transition, $\mu_{SSB}^* = 6.1$, with increasing pore width. This means that the wall separation strongly influences the biaxial ordering and, except for some specific intermediate ranges of pore width, confinement destabilizes biaxial ordering in general. For $h \gtrsim 6.6$ the curve $\mu_{UB}(h)$ interacts with the layering-transition structure and becomes discontinuous. In this case biaxiality changes the structure of the two coexisting phases at a layering transition. With increasing μ along a particular layering transition, first the phase at left of the transition curve becomes biaxial, and then

both phases show biaxial order. Therefore three types of layering transitions (U-U, U-B or B-B) can emerge in the pore.

The density and order parameter profiles for two coexisting structures of types U-B and B-B at the 5-6 layering transition are illustrated in Fig. 7. Due to commensuration effects, the density distribution of 5 layers is always less peaked than that of 6 layers. In the 5-layer structure, the pore width is a bit too spacious for the rods, while for the 6-layer structure it is too narrow. This is the case for the two coexisting structures at the general $n-n+1$ transition. Similar to the bulk biaxial smectic phase [see Fig. 3], particles are less ordered orientationally at the layers than in the interstitial regions. As the wall reduces biaxial order and therefore destabilizes the U-B phase transition, the biaxial order parameter is lowest at contact with the wall.

The interplay between biaxiality and layering transition is revealed in Fig. 8, where we demonstrate the destabilising effect of increasing the cross-sectional aspect ratio on the biaxial ordering for the 5-6 layering transition. Not surprisingly, the uniaxial-biaxial boundary curve moves down in chemical potential due to the increased molecular biaxiality. But, in addition, there is a reduction in mean density gap at the layering transition on increasing κ from 12.7 to 13.3. Also interesting is that the uniaxial phase is reentrant in a narrow range of pore widths as μ or c_0 is increased, with a phase sequence $U_5 \rightarrow B_5 \rightarrow U_6 \rightarrow B_6$. The reentrant phenomenon can be seen most clearly in the case $\kappa = 12.7$. Finally, as can be observed in Fig. 8(c), the U_5 - U_6 transition disappears by increasing the aspect ratio.

The phase diagram for the $\kappa = 17$ fluid is shown in Fig. 9. The U-B phase transition curve $\mu_{UB}(h)$ shows damped oscillatory behaviour, and in this case converges to the bulk N-NB value with increasing pore width. The destabilization effect of the walls on the U-B phase transition can be seen very clearly in this case. Since the bulk fluid now has a large region of N_B stability, and the layering transition critical points converge to $\mu_{NBSB} > \mu_{NNB}$ (see inset of Fig. 9), the U-B boundary does not intersect the layering transition curves, which now involve two biaxial phases and end in lower critical points.

Finally, we make some remarks about the reliability of Onsager theory for confined systems. It is true that the second-order virial approximation seems to be a crude approximation for dense non-uniform fluids. To assess the validity of Onsager theory, we have made a comparison between the predictions of our theory and those of our previous FMT approximation [73] formulated for the inhomogeneous fluid. In Fig. 10 we focus on a particular (15-16) layering transition; the density profiles of the two coexisting structures at the layering transition, as obtained from Onsager and FMT theories, and at a given value of μ , are shown. In Fig. 11 the locations of a few layering transitions in the μ - h phase diagrams are compared, while Fig. 12 shows density and biaxial order parameter profiles for a given chemical potential. Overall, the agreement between the two theories is quite fair. This can be understood if

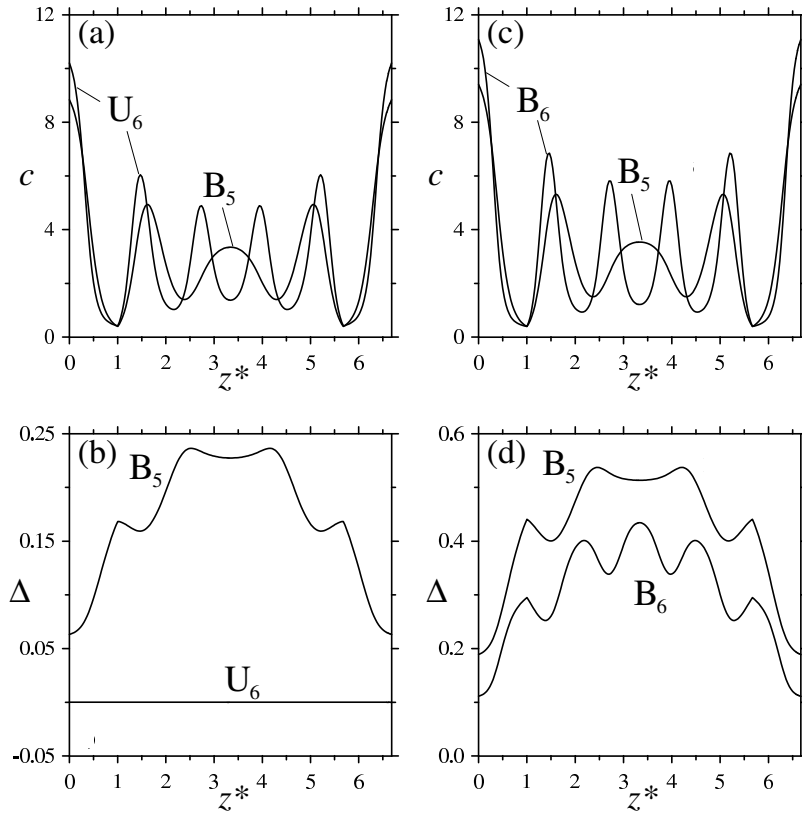


Fig. 7. Density and order-parameter profiles of coexisting structures with 5 and 6 layers. Panels (a) and (b) show profiles at the U-B layering transition with $\mu^* = 6.1$, while panels (c) and (d) correspond to those at the B-B transition with $\mu^* = 6.3$. U_5 and U_6 denote uniaxial phases with 5 and 6 layers, respectively, while B_5 and B_6 pertain to biaxial phases. The cross-sectional aspect ratio is $\kappa = 13$.

we take into account that for high aspect ratios the Onsager theory usually gives correct phase behaviour. The oscillatory structure predicted by Onsager theory is overestimated, while the width of the density peaks is a bit wider than it should be. These discrepancies are due to the poor treatment of correlations in Onsager theory. The location of the layering transitions is shifted in pore width. However, Onsager theory can be trusted as far as qualitative behaviours are concerned, and the predicted phase diagram is expected to be qualitatively correct.

4 Conclusions

We have examined the effect of confinement on the phase behaviour of a fluid of parallel biaxial hard cuboids. Using Onsager theory, four phases are observed in the bulk limit, namely uniaxial nematic, uniaxial smectic, biaxial nematic and biaxial smectic. For shape anisotropy with $\kappa < 15.304$, the sequence $N \rightarrow S \rightarrow S_B$ is observed with increasing chemical potential, while the uniaxial nematic phase transforms directly into the biaxial nematic phase for $\kappa > 15.304$, i.e. in this case the phase sequence is $N \rightarrow N_B \rightarrow S_B$.

In the fluid confined into a slit pore only two phases occur: one has uniaxial structure, while the other is biaxial. The $N-S$ transition cannot survive, but layering trans-

sitions do exist and uniaxial-biaxial phase transitions do occur. Layering transitions are associated to commensuration effects between a structure with an integer number of layers and a finite pore width, while biaxial ordering is the result of excluded-volume interactions taking place between the cross sections of the biaxial particles. Interestingly, layering transitions can be destabilized with respect to an increasing particle biaxiality, characterised by a shape parameter κ , which means that particles with a circular cross sections are the best candidates for observing layering transitions.

Layering transitions between uniaxial-uniaxial, uniaxial-biaxial, or biaxial-biaxial, structures can occur at high chemical potentials, and reentrant behaviour of the uniaxial phase may occur for increasing chemical potential and for some values of pore width. Confinement does not encourage the formation of biaxial order, since the uniaxial-biaxial phase boundary moves to higher chemical potential (density) for decreasing pore width. Therefore, for real fluids that can be modelled by this particular hard wall/fluid model system, such as colloidal suspensions of anisotropic particles, experimental detection of the biaxial nematic phase will be more favourable in bulk than in confined geometry.

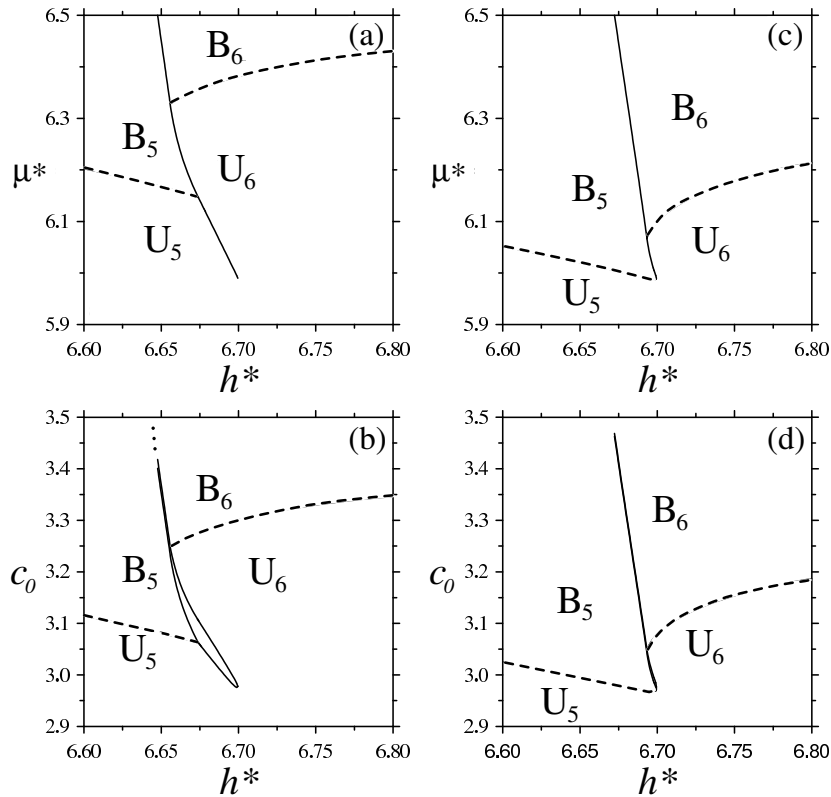


Fig. 8. Phase boundaries of layering (continuous curves) and U-B (dashed curves) phase transitions. Upper panels (a) and (c): μ^* - h^* plane. Lower panels (b) and (d): c_0 - h^* plane. U_5 and U_6 denote uniaxial phases with 5 and 6 layers, while B_5 and B_6 correspond to biaxial phases. Left panels (a) and (b): $\kappa = 12.7$; right panels (c) and (d): $\kappa = 13.3$.

Our results can be compared to those obtained earlier by van Roij et al. [16,17], who used an Onsager model in the Zwanzig (restricted orientations) approximation on hard parallelepipeds of dimensions $L \times \sigma \times \sigma$, with $L \gg \sigma$, to analyse surface and capillary behaviours. In the Zwanzig model particles can only point along the \hat{x} , \hat{y} or \hat{z} directions, and the fluid can accordingly be considered as a mixture of three species. If we take $L = \sigma_1$, our model can be related to the one in Refs. [16,17], with the important difference that, in our case, the species perpendicular to the walls is missing, so that the isotropic phase cannot occur and there is no capillary nematization/isotropization in our model (by contrast, particles can freely rotate in the xy plane, and our particle volume is finite, so that layered interfacial profiles can be obtained). As a consequence, our U-B transition occurs inside the nematic region, whereas van Roij et al. obtain it below capillary nematization (i.e. in a nematic film adsorbed on the walls), and consequently there is no dependence of the U-B transition line with pore width (in contrast with our strong oscillatory dependence, cf. Figs. 6 and 9). Our work is a step forward in the study of confined fluids of hard particles, in that layered smectic phases, not contemplated before, are included, the relationship between biaxiality and layering is ascertained, and the dependence of these phenomena with particle cross-sectional aspect ratio is analysed.

Finally, our study shows that Onsager theory can be applied for bulk and confined studies even in very ordered phases like the uniaxial or the biaxial smectic phases. Comparison of the results of Onsager with FMT theories indicates that, by including higher-order correlations into the theory, only quantitative, rather than qualitative, improvement can be achieved. We think that further studies should be performed in order to get a deeper understanding of the delicate interplay between the surface and biaxial interactions on the stability of layering, capillary and orientational transitions. It is not clear how the scenario would change if planar, instead of homeotropic, anchoring is favoured, or if the orientational entropy is included by studying fluids of freely rotating biaxial rods.

Support from Comunidad Autónoma de Madrid (grants S-0505/ESP-0299 and NANOFUID), Spain, and grants FIS2007-65869-C03-01, FIS2008-05865-C02-02 and MO-SAICO of the Ministerio de Educación y Ciencia of Spain are acknowledged.

A Bifurcation analysis

In this section we provide some analytical results for the N-S and N-N_B phase transitions of the bulk system, and also for the location of the U-B transition in the confined fluid. We also give an explanation for the peculiar

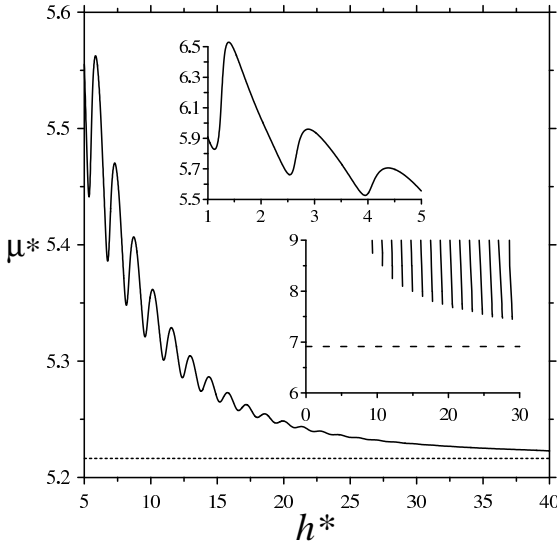


Fig. 9. Phase diagram in the $\mu^* - h^*$ plane of the U-B transition for hard cuboids of aspect ratio $\kappa = 17$. Upper inset shows detail of the same transition for small pore widths. Lower inset shows layering transitions occurring well above the U-B transition; horizontal dashed line corresponds to the bulk N_B - S_B .

behaviour of the biaxial order parameter near the S - S_B transition.

A.1 N-S bifurcation

The bifurcation analysis of the N-S phase transition of parallel hard cylinders has been discussed in earlier work [74]. Here we only present a short overview of the bifurcation analysis and show the resulting equations for the bulk bifurcation density and wavenumber of the present biaxial hard particles. The starting point is the free energy of the smectic phase, given by Eqns. (6), for a weak periodic perturbation of amplitude ϵ :

$$\rho(z) = \rho_0 (1 + \epsilon \cos qz), \quad (13)$$

where q is the wavenumber. Substitution in Eqns. (6) provides the free-energy difference ΔF between smectic and nematic phases to lowest order in ϵ :

$$\frac{\beta \Delta F}{V} = \frac{1}{4} \epsilon^2 \left[\rho_0 + 2\rho_0^2 L A_{\text{ex}}^{(0)} j_0(qL) \right], \quad (14)$$

where $j_0(x)$ is a spherical Bessel function. At the N-S bifurcation point,

$$\Delta F(\rho_0, q) = 0, \quad \frac{\partial \Delta F}{\partial q} = 0, \quad (15)$$

and the transition density results in

$$\rho_0^{\text{NS}} = -[2B_2 j_0(q_{\text{NS}}^* L)]^{-1}, \quad (16)$$

where $\pi < q_{\text{NS}}^* L < 3\pi/2$ is the smectic wave number at bifurcation, which can be obtained as a solution of the transcendental equation $\tan q_{\text{NS}}^* L = q_{\text{NS}}^* L$. The dimensionless density $c_0^{\text{NS}} = B_2 \rho_0^{\text{NS}}$ is insensitive to the particular particle model used.

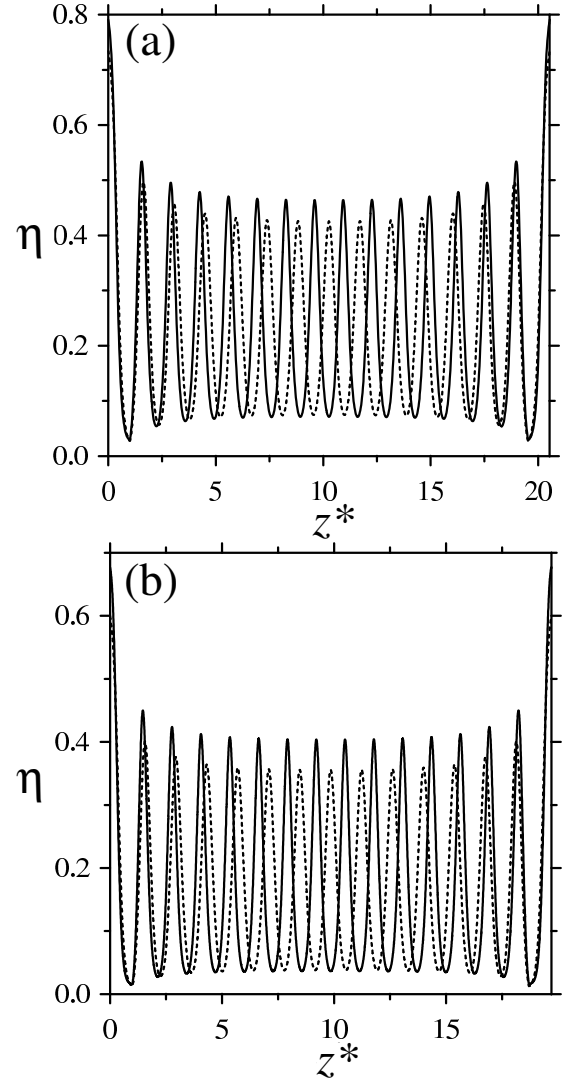


Fig. 10. Comparison of the U_{15} - U_{16} layering transition density profiles from Onsager and FMT theories for $\kappa = 13$ and $\beta\mu' = \beta\mu + \log v_0 = 3.5$. (a): Onsager theory. (b): FMT theory. The dimensionless local density is defined as $\eta(z) = \rho(z)v_0$, with $v_0 = \sigma_1\sigma_2 L$.

A.2 N- N_B bifurcation

Similar to the N-S bifurcation analysis, here we determine the free-energy cost associated with an infinitesimal biaxial ordering in the uniform nematic phase. The density distribution

$$\rho(\varphi) = \frac{\rho_0}{\pi} (1 + \epsilon \cos 2\varphi), \quad (17)$$

gives

$$\frac{\beta \Delta F}{V} = \frac{1}{4} \epsilon^2 \left[\rho_0 + 2\rho_0^2 L A_{\text{ex}}^{(1)} \right], \quad (18)$$

with $A_{\text{ex}}^{(1)} = 2\pi^{-1} \int_0^\pi d\varphi \cos 2\varphi A_{\text{ex}}(0, \varphi)$. Again the condition $\Delta F = 0$ provides a N - N_B bifurcation density, given

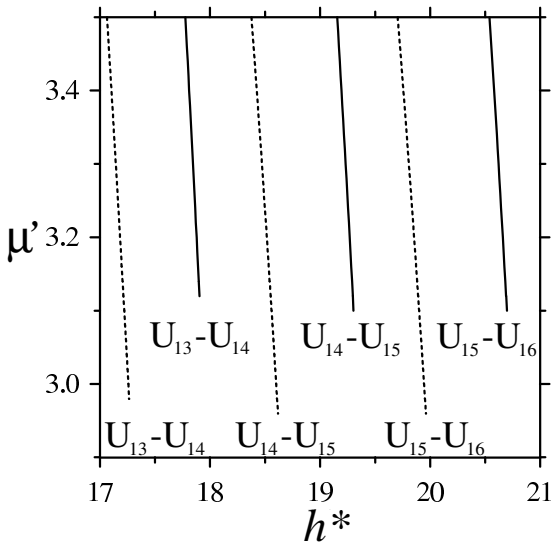


Fig. 11. Comparison of the locations of a few layering transitions in the μ' - h phase diagram for uniaxial confined structures. Continuous curves: Onsager theory. Dashed curves: FMT. $\kappa = 13$. A redefined chemical potential $\mu' = \mu^* + \log v_0$ was used.

by

$$\rho_0^{\text{NNB}} = - \left[2LA_{\text{ex}}^{(1)} \right]^{-1}, \quad (19)$$

A.3 U-B bifurcation in confined fluid

Unlike the bulk nematic phase, the confined system is nonuniform, and the uniaxial local density profile has to be determined from Eqn. (9) using a value for the chemical potential corresponding to the bifurcation point, which is not known a priori. Using Eqn. (9) it is easy to prove, by integrating out the φ dependence, that the uniaxial density distribution is the solution of the equation

$$\rho(z) = \exp \left[\beta\mu - A_{\text{ex}}^{(0)} \int_{z-a(z)}^{z+b(z)} dz_1 \rho(z_1) \right]. \quad (20)$$

The biaxial perturbation is again proportional to the function $\cos 2\varphi$, but its amplitude must depend on the position in the pore. Therefore we use the following ansatz for the perturbation:

$$\rho(z, \varphi) = \frac{\rho(z)}{\pi} [1 + \epsilon F(z) \cos 2\varphi]. \quad (21)$$

Substitution into Eqns. (6) provides a free-energy difference between the uniaxial and the biaxial confined structures, which is quadratic in ϵ . The coefficient must be zero at the bifurcation point, which provides the equation

$$\int_0^h dz \frac{f^2(z)}{\rho(z)} + \frac{A_{\text{ex}}^{(1)}}{2} \int_0^h dz_1 f(z_1) \int_{z_1-a(z_1)}^{z_1+b(z_1)} dz_2 f(z_2) = 0, \quad (22)$$

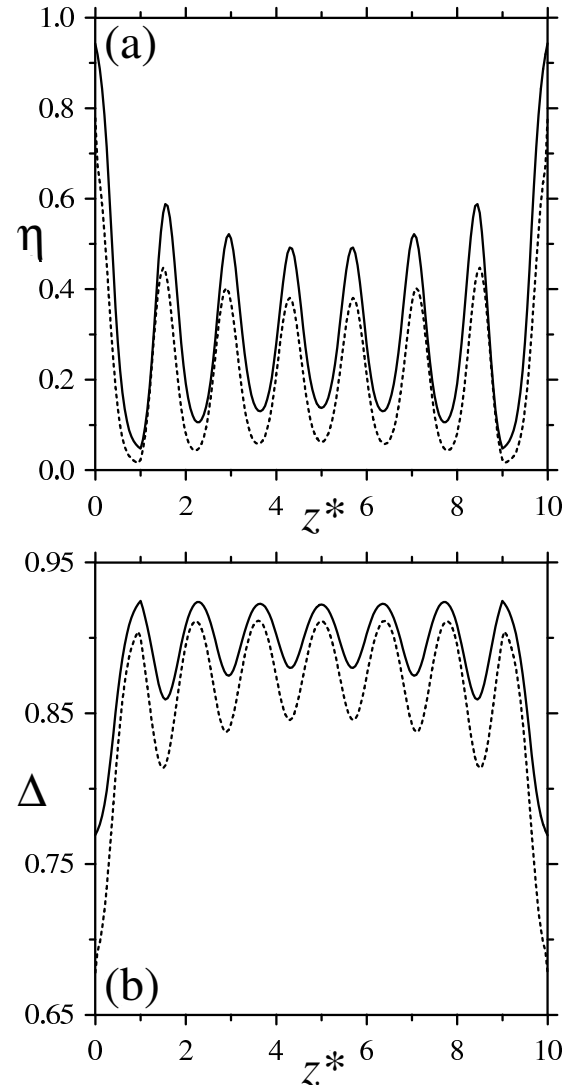


Fig. 12. Comparison of density and biaxial order parameter profiles from Onsager and FMT theories for $\kappa = 17$ and $\mu' = 4.5$ (see caption of Fig. 10). (a) Density profiles $\eta(z) = \rho(z)/v_0$. (b) Biaxial order parameter profile $\Delta(z)$. Continuous curves: Onsager theory. Dashed curves: FMT.

where $f(z) = F(z)\rho(z)$. This equation is still not suitable for the determination of $f(z)$, which requires minimizing the perturbed free energy with respect to $f(z)$. This corresponds to the functional derivative of (22) with respect to $f(z)$ being zero, i.e.

$$f(z) = -\frac{1}{2} A_{\text{ex}}^{(1)} \rho(z) \int_{z-a(z)}^{z+b(z)} dz_1 f(z_1). \quad (23)$$

The simultaneous solution of Eqns. (20), (22) and (23) gives the density profile $\rho(z)$, chemical potential μ and perturbation function $f(z)$ at the uniaxial-biaxial phase transition. From the set of U-B bifurcation equations one can get analytical results in the case $0 < h < L$. This interval corresponds to a very narrow pore, where only one monolayer of particles can fit in the pore. The upper

and lower bounds of the integral in (20) become 0 and h , respectively, i.e. the integral will give the same value for any position in the pore. This means that the local density is constant in such a narrow pore. Its value depends on the chemical potential and is given by

$$\rho(z) = \rho_0 = e^{\beta\mu} - A_{\text{ex}}^{(0)}h\rho_0. \quad (24)$$

Similar to the local density, (23) predicts a constant value $f(z) = f_0$ and a density at bifurcation given by

$$\rho_0^{\text{UB}} = -\frac{2}{hA_{\text{ex}}^{(1)}}. \quad (25)$$

Note that (25) gives the same bifurcation equation as (23). μ_{UB} can be obtained from (24) using (25).

A.4 Smectic phase biaxiality

This section is devoted to showing how the biaxial ordering of particles develops near the S-S_B transition for the particular case where the S phase is highly ordered. We explicitly show the peculiar behaviour of the order parameter profile as a periodic function peaked around the midpoint between adjacent smectic layers.

Substitution of Eqn. (21) into the definition of the biaxial order parameter, i.e.

$$\Delta(z) = \rho(z)^{-1} \int_0^\pi \rho(z, \varphi) \cos 2\varphi d\varphi \quad (26)$$

provides the result $\Delta(z) = F(z)/2$. Now insertion of the definition $f(z) = F(z)\rho(z) = 2\Delta(z)\rho(z)$ into Eqn. (23) allows us to find

$$\Delta(z) = -\frac{1}{2}A_{\text{ex}}^{(1)} \int_{z-L}^{z+L} dz_1 \rho(z_1) \Delta(z_1), \quad (27)$$

which can be viewed as an integral equation for the biaxial order parameter profile $\Delta(z)$ near the S-S_B transition. The first derivative of Eqn. (27) with respect to z gives

$$\Delta'(z) = -\frac{A_{\text{ex}}^{(1)}}{2} [\rho(z+L)\Delta(z+L) - \rho(z-L)\Delta(z-L)]. \quad (28)$$

Due to the periodicity of the order parameter profile, the function $\Delta(z \pm L)$ is periodic with period d :

$$\Delta(z \pm L) = \Delta[z \pm (L - d)]. \quad (29)$$

Its Taylor expansion about z , up to first order, gives

$$\Delta(z \pm L) \approx \Delta(z) \pm \Delta'(z)(L - d). \quad (30)$$

For the particular case of a highly ordered smectic phase (with $d \sim L$), we can make the approximation $\Delta(z \pm L) \approx \Delta(z)$, where use has been made of the fact that $\Delta'(z)$ has the same order of magnitude as $\Delta(z)$ near the bifurcation point. Note that this approximation is not justified for the

function $\rho(z \pm L)$ in general, because we have assumed that the smectic phase is highly ordered and thus that the first derivative of the density profile $\rho'(z)$ can reach high values for some values of z . Making all these approximations, we find the following differential equation for the order parameter:

$$\Delta'(z) = -\frac{A_{\text{ex}}^{(1)}}{2} \Delta(z) [\rho(z+L) - \rho(z-L)]. \quad (31)$$

The solution to this equation is

$$\Delta(z) = \Delta(0) \exp [\Psi(z) - \Psi(0)], \quad (32)$$

$$\Psi(z) = -\frac{A_{\text{ex}}^{(1)}}{2} \int_{z-L}^{z+L} \rho(z') dz'. \quad (33)$$

Assuming that the periodic density profile $\rho(z)$ is peaked at $z = z_k \equiv kd$ ($k \in \mathbb{Z}$), it is easy to show that the maxima of the function $\Psi(z)$ given by (33) are located at $z = z_k + d/2$, resulting in an order-parameter profile $\Delta(z)$ in antiphase with respect to the density profile $\rho(z)$ [see Eqns. (32) and (33)]. The present result is valid for any hard non-local interaction with a range of twice the particle length.

References

1. T. Geisinger, M. Muller, and K. Binder, *J. Chem. Phys.* **111**, 5241 (1999).
2. V. Babin, A. Ciach, and M. Tasinkevych, *J. Chem. Phys.* **114**, 9585 (2001).
3. D. de las Heras, E. Velasco and L. Mederos, *Phys. Rev. Lett.* **94**, 017801 (2005).
4. Y. Martínez-Ratón, *Phys. Rev. E* **75**, 051708 (2007).
5. H. Yokoyama, *J. Chem. Soc. Farad. T.* **84**, 1023 (1988).
6. M. M. Wittebrood, D. H. Luijendijk, S. Stallinga, Th. Rassing and I. Mušević, *Phys. Rev. E* **54**, 5232 (1996).
7. K. Kočevar, I. Mušević, *Phys. Rev. E* **64**, 051711 (2001).
8. K. Kočevar, A. Borštnik, I. Mušević and S. Žumer, *Phys. Rev. Lett.* **86**, 5914 (2001).
9. A. Borštnik Bračič, K. Kočevar, I. Mušević and S. Žumer, *Phys. Rev. E* **68**, 011708 (2003).
10. L. Moreau, P. Richetti and P. Barois, *Phys. Rev. Lett.* **73**, 3556 (1994).
11. G. R. Luckhurst, *Thin Solid Films* **393**, 40 (2001).
12. R. Berardi, L. Muccioli, S. Orlandi, M. Ricci and C. Zannoni, *J. Phys.: Condens. Matter* **20**, 463101 (2008).
13. L. A. Madsen, T. J. Dingemans, M. Nakata and E. T. Samulski, *Phys. Rev. Lett.* **92**, 145505 (2004).
14. B. R. Acharya, A. Primak and S. Kumar, *Phys. Rev. Lett.* **92**, 145506 (2004).
15. A. G. Vanakaras, S. C. McGrother, G. Jackson and D. J. Photinos, *Mol. Cryst. Liq. Cryst.* **323**, 199 (1998).
16. R. van Roij, M. Dijkstra and R. Evans, *Europhys. Lett.* **49**, 350 (2000).
17. R. van Roij, M. Dijkstra and R. Evans, *J. Chem. Phys.* **113**, 7689 (2000).
18. M. Dijkstra, R. van Roij and R. Evans, *Phys. Rev. E* **63**, 051703 (2001).

19. L. Harnau and S. Dietrich, Phys. Rev. E **66**, 051702 (2002).
20. T.J. Sluckin and A. Poniewierski, in *Fluid Interfacial Phenomena*, edited by C. A. Croxton (Wiley, New York, 1985).
21. M. M. Telo da Gama and P. Tarazona, Phys. Rev. A **41**, 11491152 (1989).
22. T. J. Sluckin, A. Poniewierski, Mol. Cryst. Liq. Cryst. **179**, 349 (1990).
23. Z. D. Zhang and W. J. Ye, Liq. Cryst. **36**, 885 (2009).
24. P. Sheng, Phys. Rev. Lett. **37**, 1059 (1976).
25. P. Sheng, Phys. Rev. A **26**, 1610 (1982).
26. T. J. Sluckin and A. Poniewierski, Phys. Rev. Lett. **55**, 2907 (1985).
27. A. Poniewierski and T.J. Sluckin, Liq. Cryst. **2**, 281 (1987).
28. E. C. Gartland, P. Palfy-Muhoray and R. S. Varga, Mol. Cryst. Liq. Cryst. **199**, 429 (1991).
29. S. Kralj, S. Žumer, and D. W. Allender, Phys. Rev. A **43**, 2943 (1991).
30. G. P. Crawford, D. W. Allender, and J. W. Doane, Phys. Rev. A **45**, 8693 (1992).
31. G. P. Crawford, R. Ondris-Crawford, S. Žumer, and J. W. Doane, Phys. Rev. Lett. **70**, 1838 (1993).
32. G. S. Iannacchione, G. P. Crawford, S. Žumer, J. W. Doane and D. Finotello, Phys. Rev. Lett. **71**, 2595 (1993).
33. M. C. J. M. Vissenberg, S. Stallinga, and G. Vertogen, Phys. Rev. E **55**, 4367 (1997).
34. P. Ziherl and S. Žumer, Phys. Rev. Lett. **78**, 682 (1997).
35. P. Ziherl, F. Karimi Pour Haddadan, R. Podgornik and S. Žumer, Phys. Rev. E **61**, 5361 (2000).
36. G. Panasyuk and D. W. Allender, J. Appl. Phys. **91**, 9603 (2002).
37. P. Palfy-Muhoray, E. C. Gartland, and J. R. Kelly, Liq. Cryst. **16**, 713 (1994).
38. H. G. Galabova, N. Kotekar and D. W. Allender, Liq. Cryst. **23**, 803 (1997).
39. A. Šarlah and S. Žumer, Phys. Rev. E **60**, 1821 (1999).
40. C. Chiccoli, P. Pasini, A. Šarlah, C. Zannoni, and S. Žumer, Phys. Rev. E **67**, 050703 (2003).
41. G. Carbone, G. Lombardo, R. Barberi, I. Mušević and U. Tkalec, Phys. Rev. Lett. **103**, 167801 (2009).
42. P. G. De Gennes, Langmuir **6**, 1448 (1990).
43. S. Kralj and T. J. Sluckin, Phys. Rev. E **50**, 2940 (1994).
44. M. Yamashita, J. Phys. Soc. Jpn. **72** 1682 (2003).
45. M. Yasen, M. Torikai and M. Yamashita, J. Phys. Soc. Jpn. **73** 2453 (2004).
46. M. Yasen, M. Torikai and M. Yamashita, Opto-Electron. Rev. **17**, 89 (2009).
47. M. Kio, M. Torikai and M. Yamashita, Opto-Electron. Rev. **17**, 8 (2009).
48. M. M. Telo da Gama, P. Tarazona, M. P. Allen and R. Evans, Mol. Phys. **71**, 801-821 (1990).
49. P. G. Ferreira and M. M. Telo da Gama, Physica A **179**, 179-198 (1991).
50. D. Cleaver and M. P. Allen, Mol. Phys. **80**, 253-276 (1993).
51. C. Chiccoli, P. Pasini, F. Semeria, E. Berggren and C. Zannoni, Mol. Cryst. Liq. Cryst. **290**, 237 (1996).
52. C. Chiccoli, O. D. Lavrentovich, P. Pasini and C. Zannoni, Phys. Rev. Lett. **79**, 44014404 (1997).
53. P. Pasini, C. Chiccoli and C. Zannoni, in *Advances in the computer simulation of liquid crystals*, P. Pasini and C. Zannoni eds. (Kluwer, Dordrecht, 2000).
54. G. D. Wall and D. J. Cleaver, Phys. Rev. E **56**, 43064316 (1997).
55. Z. Bradač, S. Kralj and S. Žumer Phys. Rev. E **58**, 74477454 (1998).
56. T. Gruhn, M. Schoen, J. Chem. Phys. **108**, 9124 (1998).
57. S. Varga and G. Jackson, Chem. Phys. Lett. **377**, 6-12 (2003).
58. H. Steuer, S. Hess and M. Schoen, Phys. Rev. E **69**, 031708 (2004).
59. D. L. Cheung and F. Schmid, Chem. Phys. Lett. **418**, 392-396 (2006).
60. L. V. Mirantsev and E. G. Virga, Phys. Rev. E **76**, 021703 (2007).
61. D. J. Cleaver and P. I. C. Teixeira, Chem. Phys. Lett. **338**, 1 (2001).
62. I. Rodríguez-Ponce, J. M. Romero-Enrique and L. F. Rull Phys. Rev. E **64**, 051704 (2001).
63. I. Rodríguez-Ponce, J. M. Romero-Enrique and L. F. Rull, J. Chem. Phys. **122**, 014903 (2005).
64. D. de las Heras, E. Velasco and L. Mederos, J. Chem. Phys. **120**, 4949 (2004).
65. D. L. Cheung and F. Schmid, J. Chem. Phys. **120**, 9185 (2004).
66. H. Reich and M. Schmidt, J. Phys.: Condens. Matter **19**, 326103 (2007).
67. P. I. C. Teixeira, F. Barmes, C. Anquetil-Deck and D. J. Cleaver, Phys. Rev. E **79**, 011709 (2009).
68. I. Rodríguez-Ponce, J. M. Romero-Enrique, E. Velasco, L. Mederos and L. F. Rull, J. Phys.: Condens. Matter **12**, A363 (2000).
69. A. Chrzanowska, P. I. C. Teixeira, H. Ehrentraut and D. J. Cleaver, J. Phys.: Condens. Matter **13**, 4715 (2001).
70. P. I. C. Teixeira, A. Chrzanowska, G. D. Wall and D. J. Cleaver, Mol. Phys. **99**, 889 (2001).
71. D. de las Heras, E. Velasco and L. Mederos, Phys. Rev. E **74**, 011709 (2006).
72. A. G. Vanakaras, M. A. Bates and D. J. Photinos, Phys. Chem. Chem. Phys. **5**, 3700 (2003).
73. Y. Martínez-Ratón, S. Varga and E. Velasco, Phys. Rev. E **78**, 031705 (2008).
74. B. Mulder, Phys. Rev. A **35**, 3095 (1987).